Interdependency of Subsurface Carbon Distribution and Graphene–Catalyst Interaction

Robert S. Weatherup,*,[†] Hakim Amara,[‡] Raoul Blume,[§] Bruno Dlubak,[∥,◆] Bernhard C. Bayer,[†] Mamadou Diarra,[⊥,#] Mounib Bahri,[‡] Andrea Cabrero-Vilatela,[†] Sabina Caneva,[†] Piran R. Kidambi,[†] Marie-Blandine Martin,[∥,◆] Cyrile Deranlot,[∥,◆] Pierre Seneor,[∥,◆] Robert Schloegl,[▽] François Ducastelle,[‡] Christophe Bichara,[⊥] and Stephan Hofmann[†]

[†]Department of Engineering, University of Cambridge, Cambridge CB3 0FA, United Kingdom
[‡]Laboratoire d'Etude des Microstructures, ONERA-CNRS, BP 72, 92322 Châtillon cedex, France
[§]Helmholtz-Zentrum Berlin für Materialien und Energie, D-12489 Berlin, Germany
[∥]Unité Mixte de Physique CNRS/Thales, 91767 Palaiseau, France
[⊥]Aix-Marseille Université CNRS, CINaM UMR 7325, 13288 Marseille, France
[#]Physics and Materials Science Research Unit, University of Luxembourg, L-1511, Luxembourg, Luxembourg
[▽]Fritz Haber Institute, D-14195 Berlin-Dahlem, Germany
[◆]University of Paris-Sud, 91405 Orsay, France

Ⓢ *Supporting Information*

ABSTRACT: The dynamics of the graphene–catalyst interaction during chemical vapor deposition are investigated using in situ, time- and depth-resolved X-ray photoelectron spectroscopy, and complementary grand canonical Monte Carlo simulations coupled to a tight-binding model. We thereby reveal the interdependency of the distribution of carbon close to the catalyst surface and the strength of the graphene–catalyst interaction. The strong interaction of epitaxial graphene with Ni(111) causes a depletion of dissolved carbon close to the catalyst surface, which prevents additional layer formation leading to a self-limiting graphene growth behavior for low exposure pressures (10^{-6}–10^{-3} mbar). A further hydrocarbon pressure increase (to ~10^{-1} mbar) leads to weakening of the graphene–Ni(111) interaction accompanied by additional graphene layer formation, mediated by an increased concentration of near-surface dissolved carbon. We show that growth of more weakly adhered, rotated graphene on Ni(111) is linked to an initially higher level of near-surface carbon compared to the case of epitaxial graphene growth. The key implications of these results for graphene growth control and their relevance to carbon nanotube growth are highlighted in the context of existing literature.
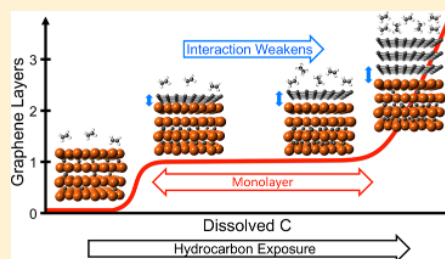
■ INTRODUCTION

Catalytic techniques for producing graphene and carbon nanotubes (CNTs), particularly those based on chemical vapor deposition (CVD), are widely seen as most promising for achieving the requisite level of control over material structure and quality that is demanded by applications.[1,2] Key to growth control is a detailed understanding of the role of the catalyst, which however remains incomplete due the wide parameter space, and more specifically for CNT CVD, the complexity of nanoparticulate catalysts.[3] There has been a great deal of recent progress in studying catalyst interactions for growing graphene on planar surfaces.[4−8] Such systems have model character in terms of catalytic CVD of all other carbon nanostructures inasmuch as flat, well-defined catalyst surfaces have been used for decades in surface science as model systems for nanoparticulate catalysts typically used in industrial heterogeneous catalysis.[3,9]

Recent literature on graphene CVD has focused on the control of nucleation density[10−13] and epitaxial[6,14,15] or pseudoepitaxial[16,17] relationships that can exist between specific catalyst surfaces and the growing graphene. It is important to note that crucial to CVD growth control is the graphene–catalyst interaction at elevated temperatures during precursor exposure. Under these reaction conditions the physical and chemical state of the catalyst surface is highly dynamic, driven by process conditions and catalyst exposure history,[6,7,18,19] and hence the graphene–catalyst interaction can be equally dynamic. Graphene on Ni(111) offers a particularly suitable model system for both theoretical and experimental investigation of the graphene–catalyst interaction during CVD. Given the 1 × 1 epitaxial match between graphene and Ni(111)

and the associated strong interaction,[5,14,20] recent literature highlights a surprisingly wide range of process-dependent graphene growth mechanisms on Ni(111),[6,21,22] some of which actually result in rotated graphene domains, indicative of a weaker catalyst interaction.[6,23] There remain significant disparities in the literature between the growth on thick single crystalline Ni(111) substrates under UHV conditions where monolayer graphene is commonly achieved,[6,14,24] and growth on polycrystalline, thin Ni films where the formation of few-layer graphene is typically reported.[25−27] Since the growth of a second or further graphene layers occurs at the interface between the catalyst and the existing graphene,[28,29] layer control is directly linked to the graphene−catalyst interaction, and this further highlights the need for understanding the variations in strength of this interaction.

Here we use in situ, time- and depth-resolved X-ray photoelectron spectroscopy (XPS)[30] and grand canonical Monte Carlo (GCMC) simulations coupled to a tight-binding (TB) model[31] to probe and rationalize the process-dependent nature of the graphene−catalyst interaction and how this relates to CVD growth control. We focus on Ni(111) as a model catalyst surface and probe in operando a wide range of hydrocarbon exposure pressures ($10^{-6}−10^{-1}$ mbar) as typically used in industrial CVD reactors. Our data reveal an interdependency between the carbon distribution close to the catalyst surface and the strength of the graphene−Ni interaction. Epitaxial graphene formation on Ni(111) leads to a depletion of carbon close to the Ni surface. This prevents the nucleation of further graphene layers and leads to a self-limiting graphene growth behavior at low exposure pressures ($10^{-6}−10^{-3}$ mbar). A further hydrocarbon pressure increase (to ∼10^{-1} mbar) leads to weakening of the graphene−Ni(111) interaction accompanied by additional graphene layer formation, mediated by an increased concentration of near-surface dissolved carbon. We show that growth of more weakly adhered, rotated graphene on Ni(111) is linked to an initially higher concentration of near-surface carbon. This allows us to consistently explain previous graphene CVD results in the literature. We further discuss the key implications for graphene growth control as well as the relevance of these results to CNT CVD.

■ RESULTS

Graphene Formation and Stability. We experimentally investigate graphene formation and stability on 40 nm thick Ni(111) films supported on monocrystalline sapphire(0001) substrates (see Figure 1 and Methods). Reflection high-energy electron diffraction (RHEED) confirms the uniform surface orientation of the catalyst (Figure 1). The samples are exposed to C_2H_4 ($10^{-6}−10^{-1}$ mbar) at 400 °C, following a pre-annealing step typically performed at 400 °C in H_2 (1 mbar) (see Methods). We emphasize that graphene growth occurs at temperature during the hydrocarbon exposure, and precip-itation on cooling is negligible, as expected for the catalyst thickness and growth temperature used.[10,27,32] The epitaxial relationship between the sapphire(0001) and Ni(111) averts the dewetting normally expected for such thin catalyst films, even following graphene growth, as confirmed by atomic force microscopy (AFM) measurements which reveal a low rms roughness of only ∼0.7 nm. We focus here on relatively thin Ni films, which allow the level of dissolved carbon throughout the catalyst to be increased more readily during hydrocarbon exposure than is possible with thicker Ni.
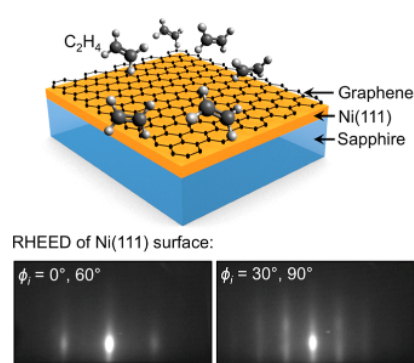

Figure 1. Schematic outlining the general growth scenario of graphene formation on 40 nm thick Ni(111) supported on sapphire(0001) during C_2H_4 exposure. RHEED patterns acquired from the Ni(111) surface, with azimuthal angles of $\phi_i = 0°$ (corresponding to the Ni [-121] azimuth) and $\phi_i = 30°$ (corresponding to the Ni [011] azimuth) with similar patterns observed at the $\phi_i = 60°$ and $\phi_i = 90°$ respectively. The incident electron energy is 18.5 keV, and the angle of incidence is 3° relative to the surface.

To help rationalize our experimental findings, we also perform GCMC simulations of graphene formation and stability on Ni(111) slabs for different temperatures (800−1200 K) and carbon chemical potentials ($\mu_C = -7.5$ to -5.0 eV/atom) (see Methods). μ_C is thereby referenced to a fictitious, ideal, monatomic gas and thus has values of similar order to the cohesive energies of the various carbon phases (e.g., −7.41 eV/atom for a graphene layer in our model). We note that for these simulations, increases in μ_C correspond qualitatively to experimental increases in hydrocarbon exposure pressure. Additionally, given the melting temperature obtained for pure bulk Ni is ∼15% higher than the experimental value,[33] the temperatures imposed in our simulations of 800−1200 K should be rescaled accordingly and thus correspond to ∼400−750 °C experimentally.

Figure 2A−D shows in situ, time-resolved XP C1s core level spectra measured on the Ni(111) surfaces during C_2H_4 (10^{-6} mbar) exposure at ∼400 °C (see Methods). In this context, time-resolved refers to scan times of tens of seconds, while the observed growth evolution proceeds over hours. We assign four principal components, which have been systematically refined on the basis of extensive CNT[19,34,35] and graphene[7,10,13,27] growth experiments and previous literature:[36−40] C_A (283.2 eV) relates to carbon bonded at Ni surface sites, C_{Dis} (283.8 eV) to interstitial carbon dissolved in the Ni lattice,[10] C_{Gr} (284.4 eV) to relatively weakly interacting graphene layers (including rotated graphene, additional graphene layers, or graphene decoupled from the Ni surface),[6,23] and C_B (284.8 eV) to strongly interacting epitaxial graphene on Ni(111).[6] We thus define the strength of the graphene−catalyst interaction on the basis of this shift in binding energy between C_{Gr} and C_B.

On exposure of the clean Ni surface (Figure 2A) to C_2H_4 (10^{-6} mbar), we observe the same C1s peak evolution as we previously reported for the growth on thick (∼1 mm) Ni(111) single crystals under similar growth conditions.[6] The C_A peak emerges ∼1 min after hydrocarbon introduction, gradually growing in intensity over ∼10 min (Figure 2B), and for these conditions is assigned to a structural surface carbide, Ni_2C.[6] A small contribution from a species at lower binding energy (∼282.9 eV) is also observed, which may reflect carbon in a different bonding environment at the Ni surface. As the C_2H_4
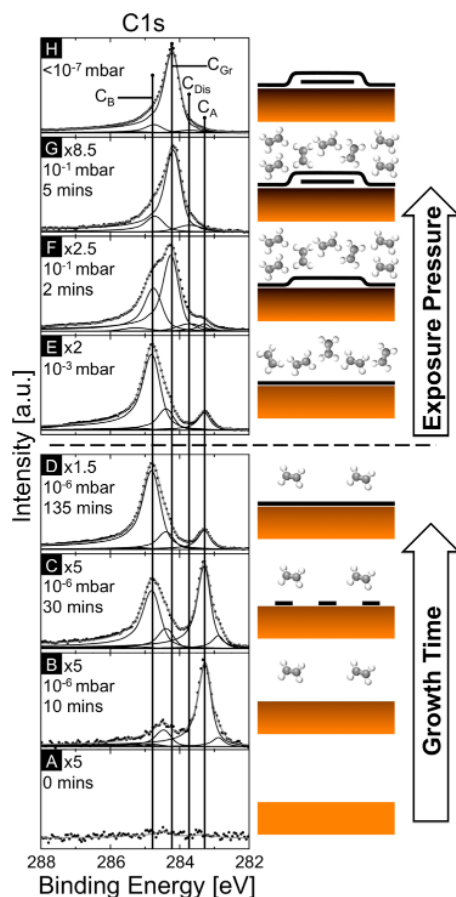
Figure 2. Time-resolved in situ XPS C1s core level spectra for Ni(111) (40 nm) [preannealed at 400 °C in H_2 (1 mbar)] during C_2H_4 exposure at 400 °C, collected at photon energies of 425 eV ($\lambda_{escape} \approx 7$ Å). Spectra are shown prior to (A) and during an initial growth exposure [C_2H_4 (10^{-6} mbar)] after 10 min (B), 30 min (C), and 135 min (D). Salient spectra acquired for subsequent stepwise increases in pressure [10^{-5}, 10^{-3}, and 10^{-1} mbar, each for ~15 min length] are shown during the 10^{-3} mbar exposure (E), the 10^{-1} exposure (F, G measured 2, 5 min respectively from the start of the pressure increase), and following subsequent removal of the C_2H_4 atmosphere (H). The spectra are normalized to have the same maximum intensities and are therfore scaled by ~5 (A–C), ~1.5 (D), ~2 (E), ~2.5 (F), and ~8.5 (G). Times signatures are relative to when the pressure started to be increased to the target value, we note that for panel F the target pressure has not yet been reached.

exposure continues, the C_B peak emerges (Figure 2C) and grows in intensity at the expense of the C_A peak and eventually becomes dominant (Figure 2D). A weak C_{Gr} peak is also present but remains a minority component throughout. The observed growth mode is thus the formation of epitaxial monolayer graphene via the transformation of Ni_2C.[6] The C_{Dis} peak also remains rather weak, as expected in light of the low solubility of carbon in Ni at this temperature.[32] The XP spectrum changes little during further exposure, indicating the stability of this epitaxial graphene monolayer under these conditions.

Figure 2E–G shows the effect on the as-formed graphene sample of stepwise increases in the C_2H_4 exposure pressure from 10^{-6} to 10^{-1} mbar. We note that increasing exposure pressures correspond to an increased carbon supply to the

catalyst surface fed through defects in the as-formed graphene,[41–44] which may include atom vacancies, substitutional catalyst atoms,[6] Stone–Wales-like defects,[45] and line[46]/grain-boundary defects. Up to 10^{-3} mbar, there is a slight decrease in total XP signal related to increasing scattering of the photoelectrons by gas molecules, however the relative intensities of the spectral components remain constant (Figure 2E). We thus confirm no significant change in the epitaxial graphene despite an increase in the feedstock pressure by 3 orders of magnitude, demonstrating that epitaxial monolayer graphene is stable across a broad pressure window.

On increasing the exposure pressure further to 10^{-1} mbar, the XP signal decreases significantly as the scattering of the photoelectrons becomes more severe.[30] Most importantly, however, a significant shift in the majority peak from C_B toward C_{Gr} occurs as the exposure proceeds (Figure 2 F,G). A notable increase in the intensity of the C_{Dis} peak is also simultaneously observed, reflecting an increase in the quantity of interstitial carbon dissolved in the Ni lattice close to the surface.[10] On removal of the C_2H_4 (10^{-1} mbar) and subsequent pumping to $<10^{-7}$ mbar (Figure 2H), the XP signal intensity is recovered, but the shift toward the C_{Gr} is retained, confirming that it is not simply an artifact of the relatively high-pressure gas environment. We also observe no such shift following exposure of epitaxial graphene on Ni(111) to atmospheric conditions and thus exclude the possibility of this shift being simply related to gas pressure. Therefore, we attribute the enduring shift to a weakening of the epitaxial graphene–Ni(111) interaction. We note similar shifts associated with weakening of the graphene–catalyst interaction are observed during post-growth annealing of graphene–Ni stacks with Au(1 nm) evaporated on top (not shown) due to Au intercalation,[10,47] and on exposure of graphene grown on Cu to atmosphere where oxygen intercalates between the graphene and Cu surface.[7]

Comparison of the absolute spectral intensities before (Figure 2D) and after (Figure 2H) the higher pressure exposure highlights that the extent of the increase in C_{Gr} peak intensity (~1.6×) is not fully accounted for by the depletion of C_B. This indicates that the weakening of the epitaxial graphene–Ni interaction is also accompanied by the formation of additional graphene layers as schematically indicated in Figure 2. As well as a supply of carbon, the formation of such additional layers requires direct contact with the catalyst.[41,48,49] Therefore, the weakening of the interaction between the first graphene layer and the catalyst enables the nucleation and insertion of additional layers between them. A modest shift (0.1–0.2 eV) in the C_{Gr} peak position toward a lower binding energy is also observed, which may reflect the even weaker interaction with the catalyst of these additional graphene layers or the graphene layers above them, relative to the small amount of rotated graphene initially present.

Figure 3 shows adsorption isotherms for carbon on Ni(111) at temperatures of 800, 1000, and 1200 K, summarizing the outcomes of GCMC simulations across different values of μ_C. The shapes of the isotherms are broadly similar for different temperatures, but with the positions of the salient points occurring at different values of μ_C. For low values of μ_C, no carbon is stable on the catalyst surface and is thus only incorporated within the catalyst as dissolved carbon. As μ_C is increased, carbon becomes stable at the Ni(111) surface, and distinct plateaus in carbon coverage can be seen which correspond to the formation of a complete epitaxial graphene monolayer on top of the Ni(111). At higher μ_C, the number of
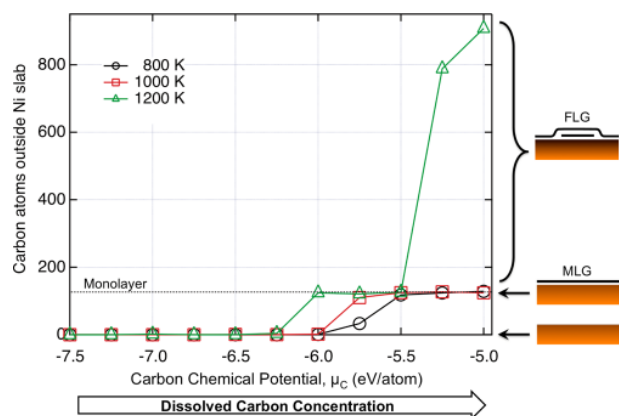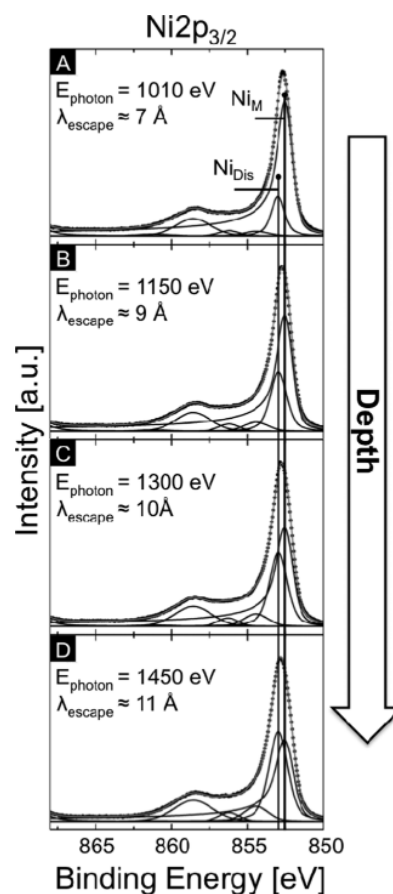
Figure 3. Adsorption isotherms for C on Ni(111) calculated on the basis of GCMC simulations performed for different C chemical potentials at 800 K (black), 1000 K (red), and 1200 K (green). These calculations were performed starting from a bare Ni surface without any graphene nucleus.

Figure 4. Depth-resolved in situ XPS Ni2p$_{3/2}$ core level lines for the Ni(111) (40 nm) during C$_2$H$_4$ exposure (10^{-6} mbar), measured directly after the C1s spectra of Figure 2D [i.e. ~135 min exposure] collected at photon energies, E_{photon}, of 1010 (A), 1150 (B), 1300 (C), and 1450 eV (D) [respective $\lambda_{escape} \approx$ 7, 9, 10, and 11 Å].

stable carbon atoms outside the Ni slab shows a sharp increase (see 1200 K isotherm), with no further plateaus observed.

This is in strong qualitative agreement with our experimental XPS findings, revealing that monolayer coverage is stable across a range of carbon chemical potentials/exposure pressures and the incorporation of additional carbon into the catalyst does not immediately lead to formation of additional graphene layers, i.e., formation of an epitaxial graphene monolayer on Ni(111) is self-limited in a certain regime. Assuming an ideal behavior of the gas phase, the plateau widths (0.5–1.0 eV) match well with the 3 orders of magnitude range of experimental feedstock pressures over which monolayer graphene is found to be stable. Indeed, given $\Delta\mu = k_B T \ln(P_1/P_2)$, a 3 orders of magnitude pressure range corresponds to a plateau width of ~0.59 eV at 1000 K. We attribute this stability of monolayer graphene to the strong interaction between the graphene and Ni, which suppresses additional layer formation. We also highlight the similarity to the monolayer phase stability across a reasonably broad temperature range, observed by Eizenberg et al. during carbon precipitation experiments with much thicker Ni(111) samples that were equilibrated over long time scales (i.e., weeks).[50]

Near-Surface Carbon Distribution. Figure 4 shows depth resolved Ni2p$_{3/2}$ core level spectra (see Methods) for the graphene covered Ni(111) sample following the formation of monolayer epitaxial graphene, during continuing C$_2$H$_4$ exposure at the growth temperature. Depth resolution is achieved by varying the incident X-ray energy, E_{photon}, which leads to an increase in the kinetic energy of photoelectrons and a corresponding increase in their mean escape depth, λ_{escape}. Two major spectral components are present in all the spectra, Ni$_M$ (~852.6 eV) and Ni$_{Dis}$ (~853.0 eV), which correspond to metallic Ni and an interstitial solid solution of carbon in Ni, respectively.[10,27] Comparison of the spectra acquired with increasing E_{photon} (Figure 4A–D) reveals that the relative intensity of the dissolved carbon species (Ni$_{Dis}$) is lowest for the most surface sensitive spectrum (Figure 4A) and increases significantly in intensity for the more depth sensitive spectra (see Figure 4D). This indicates that there is a depletion of the dissolved carbon content close to the graphene covered Ni(111) surface compared to that deeper within the sample.

Videos 1–4 (see Supporting Information) show top and side views of the atomic configurations of a Ni(111) slab during GCMC simulations performed at 1000 K with μ_C of −6.75, −6.55, −6.00, and −5.50 eV/atom, respectively, starting from a graphene nucleus of two adjacent hexagonal rings lying flat on the surface. This starting point improves the convergence of the calculations by overcoming the graphene nucleation barrier which, given the limited slab size, can be difficult to access through MC simulations. The values of μ_C at which graphene forms are thereby slightly lowered compared to Figure 3. Video 3 (see Supporting Information) exemplifies the monolayer graphene formation achieved for a certain range of μ_C (see Figure S1 of the Supporting Information for selected frames). We first observe the formation of linear carbon chains attached to the graphene nucleus and bound to the Ni surface. As growth continues, these mobile chains incorporate further C atoms, and additional graphene rings are thus added to the nucleus. Eventually nearly the whole Ni(111) surface is covered with a graphene monolayer that is in registry with the underlying Ni.

Figure 5 shows the final equilibrium configurations obtained, corresponding to Videos 1–4 (see Supporting Information). For ease of discussion, we define subsurface (1) and subsubsurface (2) interstitial sites as those located respectively between the first and second; and the second and third Ni(111)
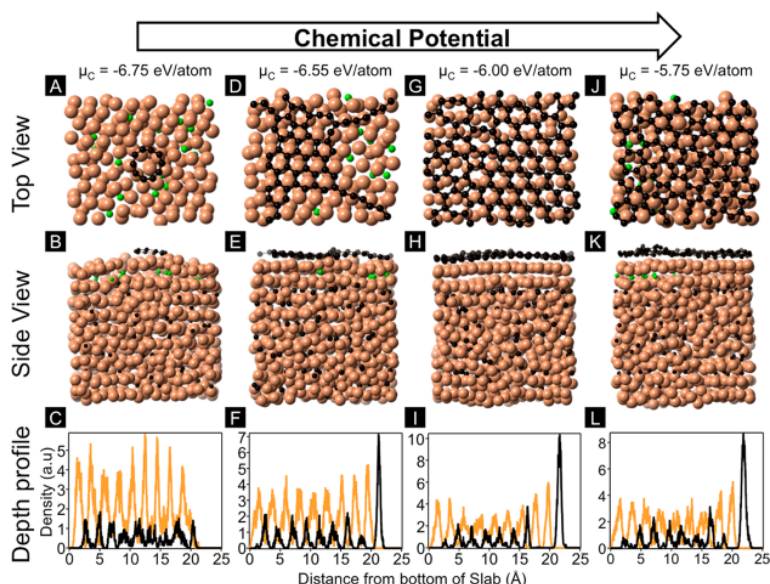
Figure 5. Top views (A, D, G, J), side views (B, E, H, K), and depth profiles (C, F, I, L) of the equilibrium structures obtained from GCMC simulations performed at 1000 K for different C chemical potentials, [$\mu_C = -6.75$ (A–C), -6.55 (D–F), -6.00 (G–I), and -5.50 (J–L) eV/atom]. A 10 atom (2 adjacent hexagons) cluster lying flat on the Ni surface was included as a nucleus, resulting in lower chemical potential values required to grow graphene, as compared to Figure 3. The top and side views show Ni atoms in orange and C atoms in black, except those C atoms in subsurface sites, which are green. The depth profiles show the Ni density as an orange line and the C density as a black line.

planes from the surface, both of which provide a full octahedral environment (see Figure 6). At $\mu_C = -6.75$ eV/atom (Figure
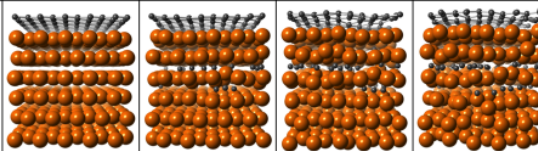

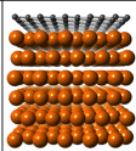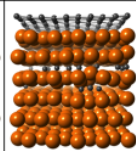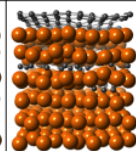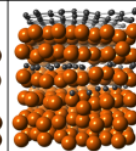| d (Å)	$\Delta E_{1\text{-}2}$ (eV)
3.5	-0.90
2.0	-0.10
1.8	+0.31
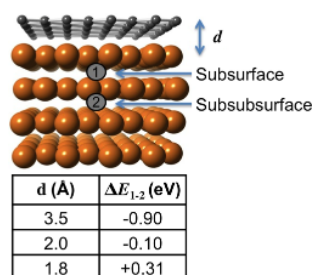
Figure 6. Side view of the epitaxial graphene covered Ni(111) slab with the positions of subsurface (1) and subsubsurface (2) interstitial sites indicated. DFT calculated carbon dissolution energies (ΔE_{1-2}) for different separations between the epitaxial graphene and Ni(111) surface (d) are tabulated.

5A–C, Video 1, see Supporting Information), no graphene is formed, and only a ring consisting of 10 C atoms is present at the Ni(111) surface. Dissolved carbon is distributed throughout the thickness of the slab, located at interstitial sites. With $\mu_C = -6.55$ eV/atom (Figure 5D–F, Video 2, see Supporting Information), partial coverage of the surface with graphene is achieved. The total number of C atoms dissolved within the Ni lattice is increased, however its distribution is notably altered with the proportion of C atoms in subsurface sites significantly reduced, compared to the distribution throughout the rest of the slab. The top view further reveals that dissolved carbon only occupies subsurface sites that are not directly below the graphene layer. A further increase of μ_C to -6.00 eV/atom (Figure 5G–I, Video 3, see Supporting Information) leads to complete coverage of the Ni(111) surface with monolayer graphene. Interestingly, no C atoms are present in subsurface

sites, while carbon remains distributed throughout the rest of the catalyst. This is qualitatively consistent with our XPS observations of a depletion of dissolved carbon content close to the graphene covered Ni(111) surface, but more specifically highlights that the presence of monolayer graphene at the Ni surface results in the depletion of carbon in the subsurface sites below. For a higher μ_C of -5.75 eV/atom (Figure 5J–L, Video 4, see Supporting Information), complete monolayer graphene coverage is again achieved at the Ni(111) surface. Subsurface sites are still depleted of carbon relative to the bulk of the Ni slab, however there are now a few C atoms present. This is attributed to the increase in the quantity of dissolved C atoms with increasing μ_C, which cannot all be accommodated in the bulk.

The graphene-induced depletion of subsurface carbon is somewhat surprising, given that bare Ni(111) interstitial sites close to the catalyst surface are expected to be more favorable for carbon incorporation than bulk sites, as the Ni lattice is able to accommodate larger local relaxations. Indeed, the typical Ni–C bond length is ~ 2.0 Å, whereas the available distance in fcc octahedral sites is $a/2 = 1.76$ Å.[51] Static TB calculations (see Methods) of the energy difference between a C atom occupying a subsurface and a subsubsurface site (ΔE_{1-2}) in the Ni(111) slab indicate that without graphene the subsurface position is most stable ($\Delta E_{1-2} = -0.9$ eV), while with an epitaxial graphene layer the subsubsurface position is preferred ($\Delta E_{1-2} = +0.8$ eV), corroborating the results of our in situ XPS experiments and GCMC simulations. It is important to note at this point that our TB model overestimates graphene adhesion energy as -0.36 eV/atom C compared to ab initio values of -0.01 to -0.05 eV/atom C.[52] Therefore, to further validate our TB results and confirm the transferability of our potential, we perform similar calculations using density functional theory (DFT) formalism at different graphene–Ni distances, which correspond to different adhesion energies, as shown in Figure 6. While subsurface sites are found to be more stable when the

	C concentration (atom %)	0	5	10	15
	Occupied Subsurface Sites (%)	0	2	4	6
	Occupied Subsubsurface Sites (%)	0	20	42	58
	Adhesion Energy (eV/C atom)	-0.35	-0.29	-0.19	-0.16

Figure 7. Side views of arrangement obtained from GCMC simulations in which C was incrementally added to an epitaxial graphene covered Ni(111) slab to give different carbon concentrations (0, 5, 10, and 15%). The corresponding values of the subsurface and subsubsurface site occupation and calculated adhesion energies of the epitaxial graphene layer are tabulated.

graphene is further from the Ni(111) surface (i.e., more weakly interacting), as the graphene layer is brought into closer proximity (i.e., more strongly interacting) there is a change in the sign of ΔE_{1-2} indicating that subsurface carbon becomes less stable and that dissolution of carbon into the catalyst bulk is preferred.

To investigate this further, we consider an epitaxial graphene covered Ni slab containing one C atom in either a subsurface or subsubsurface position. In both cases, the distance between the epitaxial graphene layer and the Ni(111) surface following relaxation is ~2 Å, which corresponds well with experimental and theoretical values typically reported in literature.[5,14,23] With a C atom occupying a subsubsurface position, the total energies of the six surrounding Ni atoms are very similar, lying between −4.71 and −4.68 eV/atom. In contrast, with a C atom occupying a subsurface position the three adjacent Ni atoms closest to the graphene layer are destabilized, with an energy loss of ~0.23 eV/atom. This effect can be understood in terms of the charge transfer from sp states of C toward d states of Ni (See Supporting Information). In the case of carbon occupying a subsubsurface position, the charge transfer is ~0.30 electrons. For the subsurface position, the different carbon environments of the three surface Ni atoms due to the presence of graphene lead to an increase in the charge transfer to ~0.75 electrons, which fills the antibonding states and therefore reduces the stability of the subsurface position.

Additional Layer Formation. We now consider in more detail the role of dissolved carbon in weakening the graphene interaction with the Ni surface. Figure 7 shows the graphene adhesion energies and resulting dissolved carbon distribution resulting from GCMC simulations in which C atoms are incrementally added to a Ni(111) slab covered with an existing epitaxial graphene monolayer. This shows that there is a decrease in the graphene adhesion energy with increasing carbon concentration within the Ni slab. Such a modification in the presence of C atoms has also been observed by Kozlov et al. using DFT calculations.[5] This is in close agreement with our experimental observations of the weakening of the epitaxial graphene−Ni(111) interaction for high hydrocarbon exposure pressures, i.e., increased carbon incorporation into the Ni. Interestingly, in spite of this reduced graphene−catalyst interaction, the subsurface remains depleted of carbon relative to the subsubsurface (see Figure 7). This therefore indicates that although dissolved carbon leads to the reduced graphene−catalyst interaction, the extent of this reduction does not result in a complete return to the carbon distribution expected if no

graphene were present. Similarly, for polycrystalline Ni films covered with predominantly nonepitaxial graphene, where the graphene−catalyst interaction is weaker than for epitaxial graphene, subsurface carbon depletion is still experimentally observed.[10,27]

Further calculations of the graphene adhesion energy, but for cases where carbon atoms are either inserted exclusively at subsurface sites or exclusively at subsubsurface sites, reveal that the occupation of either type of site results in a reduction in the graphene adhesion energy (see Supporting Information). The reduction associated with carbon in subsurface sites is however ~4 times greater than for a similar occupation of subsubsurface sites. Our GCMC simulations indicate however that for a broad range of carbon concentrations within the Ni, there are around 10 times more carbon atoms in subsubsurface sites than subsurface sites (see Figure 7). Thus, while occupation of both subsurface and subsubsurface sites contributes to the observed reduction in adhesion energy, we conclude that the carbon atoms in subsubsurface sites are for the most part responsible.

Rotated Graphene Formation. Figure 8 shows in situ, time-resolved XP C1s core level spectra growth under similar conditions as shown in Figure 2, but on a Ni(111) (40 nm) film already well filled with carbon prior to growth. This resulted from an apparently higher level of adventitious carbon present in the as loaded sample, meaning that preannealing at a higher temperature of 600 °C, rather than the typical 400 °C, was necessary to achieve a surface free of detectable carbon species in the C1s XP spectrum. However, on cooling to the growth temperature of 400 °C, a C_A peak emerges indicating the formation of regions of the structural surface carbide Ni_2C by precipitation on cooling (Figure 8A). Therefore, from the start of the growth process there is a C_A peak present that does not noticeably increase in intensity on C_2H_4 (10^{-5} mbar) exposure. Some time after the introduction of C_2H_4, C_B and C_{Gr} peaks emerge apparently simultaneously and grow in intensity with continuing exposure (Figure 8B−F). The species have similar intensities initially, however C_{Gr} becomes the stronger component as growth proceeds. As the C_B peak grows the C_A peak is depleted, which for these conditions corresponds to a growth mode in which Ni_2C is transformed into epitaxial graphene.[6] The simultaneous growth in the C_{Gr} peak intensity indicates the concurrent formation of rotated graphene, which we have previously shown to occur without the direct involvement of Ni_2C.[6] Again, as growth proceeds, there is a modest shift (0.1−0.2 eV) in the C_{Gr} peak position toward a lower binding energy, which may reflect formation of additional
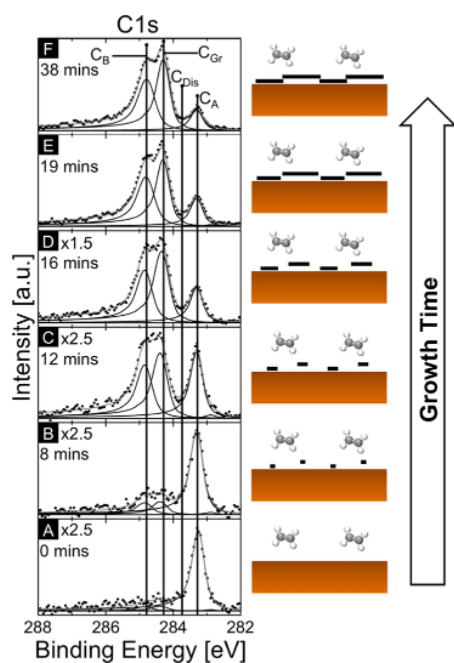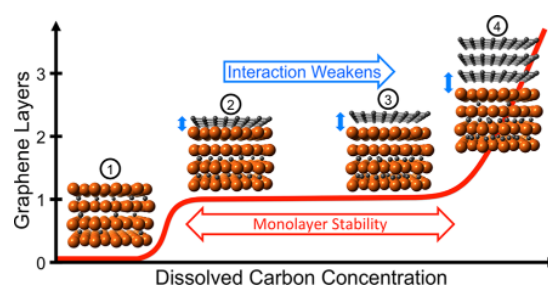
Figure 8. Time-resolved in situ XPS C1s core level lines for initially C contaminated Ni(111) (40 nm) [preannealed at 600 °C in H_2(1 mbar)] during C_2H_4 (10^{-5} mbar) exposure at 400 °C, collected at photon energies of 425 eV ($\lambda_{escape} \approx 7$ Å). The spectra are normalized to have the same maximum intensities and are therfore scaled by ~2.5 (A−C) and ~1.5 (D). Acquisition times are relative to the start of C_2H_4 exposure.

Figure 9. Schematic illustrating the interdependent variations in the graphene−Ni(111) interaction and carbon distribution, for increasing dissolved carbon concentration within the catalyst. (1) Prior to graphene formation, incorporation of carbon into subsurface interstitial sites is preferred relative to those deeper within the catalyst. (2) The formation of an epitaxial graphene layer which interacts strongly with the Ni(111) surface leads to the subsurface carbon depletion. (3) The epitaxial monolayer graphene remains stable across a broad pressure range, again due to the strong interaction between an epitaxial monolayer and Ni(111) surface. (4) On exposure to relatively high hydrocarbon exposure pressures, carbon incorporation into the Ni leads to a weakening of the graphene−catalyst interaction allowing the formation of additional graphene layers at the graphene−catalyst interface.

layers or further weakening of interaction of the rotated graphene with the catalyst.

We thus observe a significant shift in the graphene growth mode from almost exclusively epitaxial graphene formation by Ni_2C transformation on clean Ni(111) to a mixed mode, where, in addition, rotated graphene is formed by a Ni_2C-free route when more carbon is present in the catalyst prior to growth. This is attributed to the initially higher carbon content near the surface of the Ni film, leading to formation of more weakly adhered graphene and consequently a loss of epitaxy. Dissolved carbon thus is not only implicated in weakening the interaction of already formed epitaxial graphene layers with the catalyst but also in affecting the interaction, and thus epitaxy of the graphene as it forms.

■ DISCUSSION

Our experimental and theoretical data reveal the following consistent model for the coevolution of the graphene−catalyst interaction and carbon distribution within the catalyst during graphene growth (see Figure 9). Prior to graphene formation on Ni(111), the incorporation of carbon into subsurface interstitial sites is preferred relative to subsubsurface sites or those deeper within the catalyst bulk (Case 1, Figure 9). However, following the growth of epitaxial graphene, the strong interaction between the graphene and Ni(111) surface leads to the subsurface being depleted of dissolved carbon relative to the subsubsurface (Case 2, Figure 9). The epitaxial monolayer graphene remains stable across a broad pressure range, which is again related to the strong interaction between an epitaxial monolayer and the Ni(111) surface. On exposure to relatively high hydrocarbon exposure pressures the graphene−catalyst

interaction can be weakened (Case 3, Figure 9), allowing the formation of additional graphene layers at the graphene−catalyst interface (Case 4, Figure 9). This reduction in graphene−catalyst interaction is attributed to the accumulation of dissolved carbon within the Ni catalyst. Throughout this process, the subsurface sites remain depleted of carbon relative to subsubsurface sites, meaning that C atoms occupying the latter are mainly responsible for the observed reduction in adhesion energy. The presence of dissolved carbon in the catalyst not only affects the interaction of existing graphene layers with the catalyst, but an elevated initial carbon content may also lead to rotated graphene formation.

Using this understanding of the underlying mechanism we are able to rationalize a number of typically reported growth outcomes across literature, and provide insights to guide future growth approaches. While predominantly epitaxial graphene is formed during growth on initially clean Ni(111) (See Figure 2), our results indicate that for a sample with a higher initial dissolved carbon content, the formation of significant amounts of rotated graphene is observed (See Figure 8). Across literature, the conditions where rotated graphene is more readily formed are also those under which Ni is expected to contain higher absolute concentrations of dissolved carbon. This includes CVD at higher growth temperatures,[6,15] where the solubility of carbon in Ni is increased,[32] as well as growth from Ni atop solid carbon sources,[13,21] and where carbon must diffuse through the catalyst to the Ni surface. Indeed, the difficulty in controlling the initial level of adventitious carbon dissolved in the catalyst may account for differences in the temperatures at which the onset of rotated graphene formation on thick Ni(111) single crystals is observed.[6,15] This effect is readily understood in the context of the reduction in graphene−catalyst interaction induced by dissolved carbon: High levels of dissolved carbon in the catalyst from the start of growth lead to only a weak interaction between the growing graphene and Ni, reducing the preference for an epitaxial relationship between the graphene and Ni and thus increasing the likelihood of rotated graphene formation.

The difference in interaction of epitaxial and rotated graphene with Ni(111) can also affect the formation of additional graphene layers. When cooling thick Ni(111) single crystals covered with epitaxial and rotated graphene regions, no carbon precipitation is detected beneath the epitaxial regions while the formation of Ni_2C or graphene is observed beneath rotated regions.[6,15] Similarly, our experimental and theoretical observations here (Figures 2, 3) indicate a broad hydrocarbon pressure range over which epitaxial monolayer graphene is "self-limited", i.e., additional layer formation is inhibited. Only once the interaction of the epitaxial graphene and Ni(111) is sufficiently weakened by dissolved carbon incorporation can additional graphene layers form. This indicates that in addition to graphene's role in reducing the carbon supply to the Ni catalyst by passivating its surface,[41,42] the strong interaction between the graphene and Ni is a key aspect of the self-limited growth of epitaxial graphene on Ni(111). We note that under the conditions of most surface science studies, we expect epitaxial graphene to retain this strong interaction with Ni(111), which is corroborated by the predominantly monolayer growth that is generally reported. The relatively thin (40 nm) catalyst films and high hydrocarbon exposure pressures ($\sim 10^{-1}$ mbar) used herein allow the level of dissolved carbon in the catalyst to be increased more readily than is possible with the thick (~ 1 mm) single crystal substrates and ultrahigh-vacuum conditions typically used. Indeed, reports of growth on Ni(111) at close to atmospheric pressures (with hydrocarbon partial pressures in the mbar regime) show the formation of inhomogeneous few-layer graphene.[53,54]

The growth of inhomogeneous few layer graphene that is typically observed for polycrystalline Ni catalysts,[18,25,26,55] can be explained by differences in the self-limiting behavior associated with variations in the strength of graphene−Ni interaction. On such catalyst films, there are many grain orientations that lack an epitaxial relationship with graphene, and consequently the self-limiting growth associated with a strong graphene−Ni interaction, meaning additional graphene layers can be readily formed. We note however that successful approaches have been developed to avoid such multilayer formation and achieve uniform monolayer graphene coverage, e.g., using catalyst alloying to minimize multilayer nucleation[10,13] or using thick catalyst films where diffusion into the bulk kinetically mediates monolayer graphene formation at the surface.[41] In the latter case, distinct plateaus (with exposure time) exist for increasing layer numbers.[41] This relies on a carbon flux balance at the catalyst surface, mediated by both the reduction in supply from the gas phase with increasing graphene coverage and diffusion into the catalyst bulk. Therefore, while monolayer graphene growth control based on thermodynamic stability is observed experimentally and theoretically on the thin Ni layers considered here, kinetic control of layer number is not, as the bulk does not provide a suitably large mediating carbon sink. Furthermore, in the GCMC simulations carbon continues to be incorporated into the catalyst regardless of the existing graphene coverage. We note that combining both thermodynamic and kinetic control (e.g., using thick Ni(111) substrates) may further widen the window of process conditions in which monolayer graphene can be stabilized.

In addition to understanding the formation of additional layers, the stacking of these layers is also of significant interest. We have previously observed that Bernal-stacked graphene was formed by CVD,[41] while turbostratic graphene resulted from the catalytic graphitization of solid carbon sources.[13] A key difference in each case is how the catalyst surface is supplied with carbon, which in turn affects the carbon distribution within the catalyst during growth. Further studies are thus needed to develop an understanding of how this stacking is affected by the graphene−catalyst interaction and dissolved carbon within the catalyst.

It is clear, that the distribution of dissolved carbon within the catalyst can have a significant impact upon the growth outcome in terms of epitaxy, multilayer formation, and layer stacking. We therefore highlight that controlling the level of dissolved carbon within the catalyst is of key importance in achieving a desired growth result, particularly given that we have seen that small changes in the level of adventitious carbon can have a significant impact. The development of pretreatment techniques (e.g., reactive gas annealing or plasma cleaning) that allow a desired carbon distribution within the catalyst to be reliably achieved is thus of significant interest.

Considering now the growth of CNTs, much higher precursor exposure pressures are typically required than those used in graphene CVD. We note that this is consistent with the model presented here, in that cap lift-off during CNT nucleation/growth requires the weakening of the cap-catalyst interaction, and increased carbon incorporation into the catalyst is expected to facilitate this.[56] The scenario for CNT growth is however somewhat more complex, as the forming sp^2 lattice also leads to reshaping of the catalyst particle.[34] This reshaping effect is in turn related to the carbon concentration in the catalyst as discussed in previous literature.[56−58] Furthermore, the interaction of the nanoparticulate catalyst with the support is of key importance in CNT formation,[35,59−61] and support-dependent changes in the catalyst carbon concentration and hence growth outcome have been observed.[18,62,63]

The structural reciprocity apparent in CNT growth is also highly relevant to graphene CVD, particularly where graphene grows embedded in the topmost catalyst layer[6,64] and at temperatures where the catalyst is close to its melting point and thus highly mobile. In the latter case any epitaxial or pseudoepitaxial relationship observed post-growth may in fact relate to catalyst recrystallization at the graphene interface,[16,65] and studies on this are ongoing.

■ CONCLUSIONS

In summary, we have shown that the strong interaction of epitaxial graphene with Ni(111) leads to a self-limited growth regime in which epitaxial monolayer graphene is stable for C_2H_4 exposures as high as 10^{-3} mbar. The presence of graphene alters the distribution of dissolved carbon close to the catalyst surface, and reciprocally, the dissolved carbon within the catalyst can modify the graphene−catalyst interaction. Dissolved carbon is thus implicated in the weakening of the graphene−catalyst interaction that facilitates additional layer formation as well as the loss of epitaxy that leads to rotated graphene. We are thus able to provide a consistent explanation for the apparent disparities between growth results obtained under UHV compared to near atmospheric pressure conditions. The insights obtained are of particular relevance in understanding how the interaction between a catalyst and graphene affects its growth and more broadly in understanding the role of the catalyst in the growth of nanostructured carbons.

■ METHODS

Experimental Section. We investigate Ni(111) films (40 nm thickness) deposited by sputtering a Ni target (5N purity) with a 2W/cm^2 DC plasma in a 2.5×10^{-3} mbar Ar atmosphere (6N purity, base pressure 5×10^{-8} mbar) on monocrystalline sapphire(0001) substrates (Alfa Aesar) heated to 600 °C. The resulting Ni(111) films crystallographic orientation and homogeneity were confirmed by RHEED (see Figure 1) as well as XRD, XRR, and AFM measurements. The samples are transferred in air to custom-built cold-wall reactors (base pressures <10^{-6} mbar) for graphene growth. The growth process consists of pre-annealing [typically at 400 °C in H_2 (1 mbar), heated at a constant rate of 100 °C min^{-1}], hydrocarbon exposure [400 °C, C_2H_4 ($10^{-6} - 10^{-1}$ mbar)], and then cooling [under vacuum (~10^{-7} mbar) at ~100 °C/min]. For Au intercalation reference experiments, Au(1 nm) is thermally evaporated on graphene-Ni samples ex-situ, following growth and subsequent transfer in air.

In situ XPS measurements were performed at the BESSY II synchrotron at the ISISS end station of the FHI-MPG. The high-pressure setup consists mainly of a reaction cell (base pressure ~ 10^{-7} mbar) attached to a set of three differentially pumped electrostatic lenses and a differential-pumped analyzer (Phoibos 150, SPECS GmbH), as described elsewhere.[30] All spectra are collected in normal emission geometry, with a spot size of 80 × 150 μm and spectral resolution of ~0.3 eV. Time signatures are relative to when the C_2H_4 valve is opened or adjusted. C1s spectra are collected at E_{photon} of 425 eV ($\lambda_{escape} \approx 7$ Å), while for the Ni2$p_{3/2}$ spectra E_{photon} is varied between 1010 and 1450 eV ($\lambda_{escape} \approx 7-11$ Å) to achieve depth resolution.

All spectra are background corrected (Shirley) and analyzed by performing a nonlinear mean square fit of the data, using Doniach–Šùnjić functions convoluted with Gaussian profiles with an accuracy of ~0.05 eV. All binding energies are referenced to the contemperaneously measured Fermi edge.

Theoretical. In the TB calculations, a minimal basis, including s, p electrons of C and d electrons of Ni, is required to obtain a transferable TB model of the C–C, Ni–Ni, and Ni–C interactions applicable to binary systems.[66] We use the recursion technique with a continued fraction in order to determine the local electronic density of states and thus local energy. The ability to readily analyze local energy distributions proves very useful in this study. Moreover, we impose a local charge neutrality condition. Other work using DFT calculations[67] or empirical potentials[68] is reported in the literature, however our model, with its high degree of transferability, enables large systems (~1000 atoms) to be dealt with and is fairly accurate when compared to experiment or ab initio calculations.

The TB model is then implemented in a Monte Carlo code using either a canonical or grand canonical algorithm with fixed volume, temperature, number of Ni atoms, and carbon chemical potential μ_C.[31] Simulations are performed on a nine-layer Ni slab consisting of 576 atoms in total and presenting a (111) surface. A 15 Å thick vacuum region is added along the z axis, and periodic boundary conditions are used. The box size is 19.91 × 17.24 × 36.58 $Å^3$. The GC algorithm used consists of a series of Monte Carlo cycles, each of which randomly alternates displacement moves for Ni or C atoms and attempts to incorporate new carbon atoms into, or remove existing carbon atoms. Once equilibrium is reached, we record the number of C atoms outside the slab of Ni at chosen μ_C and temperature to draw the carbon adsorption isotherms for different temperatures (800–1200 K). Applications of this model to surface segregation of carbon and to the catalytic nucleation of carbon caps have already been presented elsewhere.[51,56,69]

DFT calculations are performed using the Vienna ab initio simulation package (VASP) code within the generalized gradient approximation (GGA) exchange–correlation functionals.[70,71] Core and valence electrons are represented by a plane wave basis and projector augmented wave (PAW) potentials. All our calculations are spin polarized. The system consists of a slab of Ni (111) containing a C atom either in a subsurface or subsubsurface position, within a

supercell sufficiently large to minimize boundary effects on the energies of interest. The metal surface is simulated using a six-layer slab consisting of 54 atoms in total. When graphene is considered on Ni(111), its lattice constant (a = 2.46 Å) is scaled to fit the experimental minimal surface unit cell of Ni which has side length of 2.51 Å. Adjacent supercells in the c direction are separated by a vacuum region of about 15 Å to avoid interaction between neighboring supercells. Integration over the Brillouin zone is based on a (5 × 5 × 1) Monkhorst–Pack three-dimensional grid. Cold smearing is used for the Brillouin zone integration leading to formation energies converged to within 10^{-4} eV. The relaxation of the atoms of the simulation cell is considered using the conjugate gradient minimization scheme and stopped when the forces are <0.1 eV/Å.

■ ASSOCIATED CONTENT

ⓢ Supporting Information
Selected images from GCMC simulations corresponding to Video 3, variation in graphene adhesion energy with increasing subsurface and subsubsurface site occupation, detailed description of the reduced stability of subsurface compared to subsubsurface carbon with graphene present. Video 1−4 showing top and side views during GCMC simulation performed at 1000K for μ_C of −6.75, −6.55, −6.00, and −5.50 eV/atom respectively (corresponding to Figure 5). They are available in .mpg format in the HTML version of the paper. This material is available free of charge via the Internet at http://pubs.acs.org.

■ AUTHOR INFORMATION

Corresponding Author
rsw31@cam.ac.uk

Notes
The authors declare no competing financial interest.

■ ACKNOWLEDGMENTS

■ REFERENCES

(1) Novoselov, K. S.; Fal'ko, V. I.; Colombo, L.; Gellert, P. R.; Schwab, M. G.; Kim, K. *Nature* **2012**, *490*, 192−200.
(2) Hata, K.; Futaba, D. N.; Mizuno, K.; Namai, T.; Yumura, M.; Iijima, S. *Science* **2004**, *306*, 1362−13644.
(3) Stierle, A.; Molenbroek, A. *MRS Bull.* **2007**, *32*, 1001−1009.
(4) Larciprete, R.; Ulstrup, S.; Lacovig, P.; Dalmiglio, M.; Bianchi, M.; Mazzola, F.; Hornekær, L.; Orlando, F.; Baraldi, A.; Hofmann, P.; Lizzit, S. *ACS Nano* **2012**, *6*, 9551−9558.
(5) Kozlov, S.; Viñes, F.; Görling, A. *J. Phys. Chem. C* **2012**, *116*, 7360−7366.
(6) Patera, L. L.; Africh, C.; Weatherup, R. S.; Blume, R.; Bhardwaj, S.; Castellarin-Cudia, C.; Knop-Gericke, A.; Schloegl, R.; Comelli, G.; Hofmann, S.; Cepek, C. *ACS Nano* **2013**, *7*, 7901−7912.
(7) Kidambi, P. R.; Bayer, B. C.; Blume, R.; Wang, Z.-J.; Baehtz, C.; Weatherup, R. S.; Willinger, M.-G.; Schloegl, R.; Hofmann, S. *Nano Lett.* **2013**, *13*, 4769−4778.

(8) Dahal, A.; Batzill, M. *Nanoscale* **2014**, *6*, 2548–2562.

(9) Lundgren, E.; Over, H. J. *Phys. Condens. Matter* **2008**, *20*, 180302.

(10) Weatherup, R. S.; Bayer, B. C.; Blume, R.; Ducati, C.; Baehtz, C.; Schlögl, R.; Hofmann, S. *Nano Lett.* **2011**, *11*, 4154–4160.

(11) Li, X.; Magnuson, C. W.; Venugopal, A.; An, J.; Suk, J. W.; Han, B.; Borysiak, M.; Cai, W.; Velamakanni, A.; Zhu, Y.; Fu, L.; Vogel, E. M.; Voelkl, E.; Colombo, L.; Ruoff, R. S.; et al. *Nano Lett.* **2010**, *10*, 183–191.

(12) Hao, Y.; Bharathi, M.; Wang, L.; Liu, Y.; Chen, H.; Nie, S.; Wang, X.; Chou, H.; Tan, C.; Fallahazad, B.; Ramanarayan, H.; Magnuson, C. W.; Tutuc, E.; Yakobson, B. I.; McCarty, K. F.; Zhang, Y.-W.; Kim, P.; Hone, J.; Colombo, L.; Ruoff, R. S. *Science* **2013**, *342*, 720–723.

(13) Weatherup, R. S.; Baehtz, C.; Dlubak, B.; Bayer, B. C.; Kidambi, P. R.; Blume, R.; Schloegl, R.; Hofmann, S. *Nano Lett.* **2013**, *13*, 4624–4631.

(14) Gamo, Y.; Nagashima, A.; Wakabayashi, M.; Terai, M.; Oshima, C. *Surf. Sci.* **1997**, *374*, 61–64.

(15) Dahal, A.; Addou, R.; Sutter, P.; Batzill, M. *Appl. Phys. Lett.* **2012**, *100*, 241602.

(16) Wilson, N. R.; Marsden, A. J.; Saghir, M.; Bromley, C. J.; Schaub, R.; Costantini, G.; White, T. W.; Partridge, C.; Barinov, A.; Dudin, P.; Sanchez, A. M.; Mudd, J. J.; Walker, M.; Bell, G. R. *Nano Res.* **2013**, *6*, 99–112.

(17) Lee, J.-H.; Lee, E. K.; Joo, W.-J.; Jang, Y.; Kim, B.-S.; Lim, J. Y.; Choi, S.-H.; Ahn, S. J.; Ahn, J. R.; Park, M.-H.; Yang, C.-W.; Choi, B. L.; Hwang, S.-W.; Whang, D. *Science* **2014**, *344*, 286–289.

(18) Wirth, C. T.; Bayer, B. C.; Gamalski, A. D.; Esconjauregui, S.; Weatherup, R. S.; Ducati, C.; Baehtz, C.; Robertson, J.; Hofmann, S. *Chem. Mater.* **2012**, *24*, 4633–4640.

(19) Hofmann, S.; Blume, R.; Wirth, C. T.; Cantoro, M.; Sharma, R.; Ducati, C.; Hävecker, M.; Zafeiratos, S.; Schnoerch, P.; Oestereich, A.; Teschner, D.; Albrecht, M.; Knop-Gericke, A.; Schlögl, R.; Robertson, J. *J. Phys. Chem. C* **2009**, *113*, 1648–1656.

(20) Karpan, V. M.; Khomyakov, P. A.; Starikov, A. A.; Giovannetti, G.; Zwierzycki, M.; Talanana, M.; Brocks, G.; van den Brink, J.; Kelly, P. J. *Phys. Rev. B* **2008**, *78*, 195419.

(21) Murata, Y.; Petrova, V.; Kappes, B. *ACS Nano* **2010**, *4*, 6509–6514.

(22) Lahiri, J.; Miller, T.; Adamska, L.; Oleynik, I. I.; Batzill, M. *Nano Lett.* **2011**, *11*, 518–522.

(23) Shibuta, Y.; Elliott, J. A. *Chem. Phys. Lett.* **2012**, *538*, 112–117.

(24) Addou, R.; Dahal, A.; Sutter, P.; Batzill, M. *Appl. Phys. Lett.* **2012**, *100*, 021601.

(25) Yu, Q.; Lian, J.; Siriponglert, S.; Li, H.; Chen, Y. P.; Pei, S. S. *Appl. Phys. Lett.* **2008**, *93*, 113103.

(26) Reina, A.; Jia, X.; Ho, J.; Nezich, D.; Son, H.; Bulovic, V.; Dresselhaus, M. S.; Kong, J. *Nano Lett.* **2009**, *9*, 30–35.

(27) Weatherup, R. S.; Bayer, B. C.; Blume, R.; Baehtz, C.; Kidambi, P. R.; Fouquet, M.; Wirth, C. T.; Schlögl, R.; Hofmann, S. *ChemPhysChem* **2012**, *13*, 2544–2549.

(28) Nie, S.; Wofford, J.; Bartelt, N.; Dubon, O.; McCarty, K. *Phys. Rev. B* **2011**, *84*, 155425.

(29) Nie, S.; Wu, W.; Xing, S.; Yu, Q.; Bao, J.; Pei, S.; McCarty, K. F. *New J. Phys.* **2012**, *14*, 093028.

(30) Bluhm, H.; Hävecker, M.; Knop-Gericke, A.; Kiskinova, M.; Schlögl, R.; Salmeron, M. *MRS Bull.* **2007**, *32*, 1022–1030.

(31) Frenkel, D.; Smit, B. *Understanding Molecular Simulation*; Academic Press: London, 2002.

(32) Lander, J. J.; Kern, H. E.; Beach, A. L. *J. Appl. Phys.* **1952**, *23*, 1305–1309.

(33) Los, J. H.; Pellenq, R. J. M. *Phys. Rev. B* **2010**, *81*, 064112.

(34) Hofmann, S.; Sharma, R.; Ducati, C.; Du, G.; Mattevi, C.; Cepek, C.; Cantoro, M.; Pisana, S.; Parvez, A.; Cervantes-Sodi, F.; Ferrari, A. C.; Dunin-Borkowski, R.; Lizzit, S.; Petaccia, L.; Goldoni, A.; Robertson, J. *Nano Lett.* **2007**, *7*, 602–608.

(35) Bayer, B. C.; Hofmann, S.; Castellarin-Cudia, C.; Blume, R.; Baehtz, C.; Esconjauregui, S.; Wirth, C. T.; Oliver, R.; Ducati, C.; Knop-Gericke, A.; et al. *J. Phys. Chem. C* **2011**, *115*, 4359–4369.

(36) Díaz, J.; Paolicelli, G.; Ferrer, S.; Comin, F. *Phys. Rev. B* **1996**, *54*, 8064–8069.

(37) Morar, J.; Himpsel, F.; Hollinger, G. *Phys. Rev. B* **1986**, *33*, 1340–1345.

(38) Webb, M. J.; Palmgren, P.; Pal, P.; Karis, O.; Grennberg, H. *Carbon* **2011**, *49*, 3242–3249.

(39) Lacovig, P.; Pozzo, M.; Alfè, D.; Vilmercati, P.; Baraldi, A.; Lizzit, S. *Phys. Rev. Lett.* **2009**, *103*, 166101.

(40) Grüneis, A.; Kummer, K.; Vyalikh, D. V. *New J. Phys.* **2009**, *11*, 073050.

(41) Weatherup, R. S.; Dlubak, B.; Hofmann, S. *ACS Nano* **2012**, *6*, 9996–10003.

(42) Kidambi, P. R.; Ducati, C.; Dlubak, B.; Gardiner, D.; Weatherup, R. S.; Martin, M.-B.; Seneor, P.; Coles, H.; Hofmann, S. *J. Phys. Chem. C* **2012**, *116*, 22492–22501.

(43) Hsieh, Y.; Hofmann, M.; Chang, K.; Jhu, J.; Li, Y.-Y.; Chen, K. Y.; Yang, C. C.; Chang, W.-S.; Chen, L.-C. *ACS Nano* **2013**, *8*, 443–448.

(44) Boutilier, M. S. H.; Sun, C.; O'Hern, S. C.; Au, H.; Hadjiconstantinou, N. G.; Karnik, R. *ACS Nano* **2014**, *8*, 841–849.

(45) Stone, A.; Wales, D. *Chem. Phys. Lett.* **1986**, *128*, 501–503.

(46) Lahiri, J.; Lin, Y.; Bozkurt, P.; Oleynik, I. I.; Batzill, M. *Nat. Nanotechnol.* **2010**, *5*, 326–329.

(47) Varykhalov, A.; Sánchez-Barriga, J.; Shikin, A.; Biswas, C.; Vescovo, E.; Rybkin, A.; Marchenko, D.; Rader, O. *Phys. Rev. Lett.* **2008**, *101*, 157601.

(48) Helveg, S.; López-Cartes, C.; Sehested, J.; Hansen, P. L.; Clausen, B. S.; Rostrup-Nielsen, J. R.; Abild-Pedersen, F.; Nørskov, J. K. *Nature* **2004**, *427*, 426–429.

(49) Nie, S.; Walter, A. L.; Bartelt, N. C.; Starodub, E.; Bostwick, A.; Rotenberg, E.; McCarty, K. F. *ACS Nano* **2011**, *5*, 2298–2306.

(50) Eizenberg, M.; Blakely, J. M. *J. Chem. Phys.* **1979**, *71*, 3467–3477.

(51) Amara, H.; Bichara, C.; Ducastelle, F. *Phys. Rev. B* **2006**, *73*, 113404.

(52) Olsen, T.; Yan, J.; Mortensen, J. J.; Thygesen, K. S. *Phys. Rev. Lett.* **2011**, *107*, 156401.

(53) Dahal, A.; Coy-Diaz, H.; Addou, R.; Lallo, J.; Sutter, E.; Batzill, M. *J. Appl. Phys.* **2013**, *113*, 194305.

(54) Zhang, Y.; Gao, T.; Xie, S.; Dai, B.; Fu, L.; Gao, Y.; Chen, Y.; Liu, M.; Liu, Z. *Nano Res.* **2012**, *5*, 402–411.

(55) Kim, K. S.; Zhao, Y.; Jang, H.; Lee, S. Y.; Kim, J. M.; Kim, K. S.; Ahn, J.-H.; Kim, P.; Choi, J.-Y.; Hong, B. H. *Nature* **2009**, *457*, 706–710.

(56) Diarra, M.; Zappelli, A.; Amara, H.; Ducastelle, F.; Bichara, C. *Phys. Rev. Lett.* **2012**, *109*, 185501.

(57) Moseler, M.; Cervantes-Sodi, F.; Hofmann, S.; Csányi, G.; Ferrari, A. C. *ACS Nano* **2010**, *4*, 7587–7595.

(58) Pigos, E.; Penev, E. S.; Ribas, M. A.; Sharma, R.; Yakobson, B. I.; Harutyunyan, A. R. *ACS Nano* **2011**, *5*, 10096–10101.

(59) Mattevi, C.; Wirth, C. T.; Hofmann, S.; Blume, R.; Cantoro, M.; Ducati, C.; Cepek, C.; Knop-Gericke, A.; Milne, S.; Castellarin-Cudia, C.; Dolafi, S.; Goldoni, A.; Schloegl, R.; Robertson, J. *J. Phys. Chem. C* **2008**, *112*, 12207–12213.

(60) Bayer, B. C.; Fouquet, M.; Blume, R.; Wirth, C. T.; Weatherup, R. S.; Ogata, K.; Knop-Gericke, A.; Schlögl, R.; Hofmann, S.; Robertson, J. *J. Phys. Chem. C* **2012**, *116*, 1107–1113.

(61) Michaelis, F. B.; Weatherup, R. S.; Bayer, B. C.; Bock, M. C. D.; Sugime, H.; Caneva, S.; Robertson, J.; Baumberg, J. J.; Hofmann, S. *ACS Appl. Mater. Interfaces* **2014**, *6*, 4025–4032.

(62) Rinaldi, A.; Tessonnier, J.-P.; Schuster, M. E.; Blume, R.; Girgsdies, F.; Zhang, Q.; Jacob, T.; Abd Hamid, S. B.; Su, D. S.; Schlögl, R. *Angew. Chem., Int. Ed.* **2011**, *50*, 3313–3317.

(63) Cartwright, R. J.; Esconjauregui, S.; Weatherup, R. S.; Hardeman, D.; Guo, Y.; Wright, E.; Oakes, D.; Hofmann, S.; Robertson, J. *Carbon* **2014**, *75*, 327–334.

(64) Starodub, E.; Maier, S.; Stass, I.; Bartelt, N. C.; Feibelman, P. J.; Salmeron, M.; McCarty, K. F. *Phys. Rev. B* **2009**, *80*, 235422.

(65) Wu, Y. A.; Fan, Y.; Speller, S.; Creeth, G. L.; Sadowski, J. T.; He, K.; Robertson, A. W.; Allen, C. S.; Warner, J. H. *ACS Nano* **2012**, *6*, 5010−5017.

(66) Amara, H.; Roussel, J.-M.; Bichara, C.; Gaspard, J.-P.; Ducastelle, F. *Phys. Rev. B* **2009**, *79*, 014109.

(67) Shibuta, Y.; Arifin, R.; Shimamura, K.; Oguri, T.; Shimojo, F.; Yamaguchi, S. *Chem. Phys. Lett.* **2013**, *565*, 92−97.

(68) Neyts, E. C.; van Duin, A. C. T.; Bogaerts, A. *Nanoscale* **2013**, *5*, 7250−7255.

(69) Diarra, M.; Amara, H.; Ducastelle, F.; Bichara, C. *Phys. Status Solidi* **2012**, *249*, 2629−2634.

(70) Kresse, G.; Furthmüller, J. *Phys. Rev. B* **1996**, *54*, 11169−11186.

(71) Kresse, G.; Joubert, D. *Phys. Rev. B* **1999**, *59*, 1758−1775.